Ordinary state-based peridynamic shell model with arbitrary horizon domains for surface effect correction

Ming-Jyun Dai[a], Satoyuki Tanaka[a,*], Pai-Chen Guan[b], Selda Oterkus[c], Erkan Oterkus[c]

[a] *Graduate School of Advanced Science and Engineering, Hiroshima University, Japan*
[b] *Department of Systems Engineering and Naval Architecture, National Taiwan Ocean University, Taiwan*
[c] *Department of Naval Architecture, Ocean and Marine Engineering, University of Strathclyde, United Kingdom*

Abstract

An ordinary state-based peridynamic (PD) shell model with arbitrary horizon domains is presented. In computations of the PD parameters, the model removes the complete horizon assumption when treating the PD surface effect. In this study, the membrane, bending, and transverse shear deformations in the PD framework are taken into account. To examine fracture mechanics behavior, crack opening displacements and strain energy densities, which correspond to physical values of the PD failure criteria, are investigated under single- and mixed-mode fracture conditions. Several numerical examples are considered to evaluate fracture behaviors for shell structures subjected to in-plane or out-of-plane loading. The PD surface effect near domain boundaries or crack surfaces is validly treated. In addition, a crack propagation analysis is performed to estimate the effectiveness of the presented method.

Keywords: Peridynamics; Thin-walled structures; Arbitrary horizon domain; Surface effect; Crack propagation

*Corresponding author. E-mail addresses: mingjyundai@gmail.com (M.J. Dai), satoyuki@hiroshima-u.ac.jp (S. Tanaka), paichen@mail.ntou.edu.tw (P.C. Guan), selda.oterkus@strath.ac.uk (S. Oterkus), erkan.oterkus@strath.ac.uk (E. Oterkus)

Dai, M-J., Tanaka, S., Guan, P-C., Oterkus, S., & Oterkus, E. (Accepted/In press). Ordinary state-based peridynamic shell model with arbitrary horizon domains for surface effect correction. Theoretical and Applied Fracture Mechanics.

1.Introduction

Anonlocaltheory,peridynamics(PD)[1,2],providesanalternativeapproachtodealwithfracturemechanicsproblems.Incontrasttoclassicalcontinuummechanics(CCM),thePDtheorydoesnotinvolvespatialderivativesinthegoverningequationsandhenceiswellsuitedtotreatcomplicatedfractureproblemswithoutadditionalnumericaltechniques.ThreedifferenttypesofPDformulationshavebeenproposedinthePDliterature,specifically,bond-basedPD(BBPD)[1],ordinarystate-basedPD(OSPD)[2],andnon-ordinarystate-basedPD(NOSPD)[2].BBPDplacesconstraintsonmaterialpropertiesandplasticbehavior.Poisson'sratioisrestrictedtospecifiedvalues.Moreover,permanentdeformationonlyconsidersthevolumetricstrain;hence,itisinconsistentwithplasticincompressibilityinmetals.Therefore,OSPDandNOSPDhavebeensubsequentlydevelopedasmoregeneralformstorelaxlimitationsplacedonmaterialpropertiesandplasticsimulations.

Becauseoftheirhighstrength-to-weightratio,thin-walledstructuresarecommonlyusedinaerospaceandmaritimeindustries.InthePDframework,nonlocalinteractionsineachmaterialpointareconsideredwithothermaterialpointswithinspecifiedregions.Thenonlocalpropertyleadstolowerefficienciesincomputationtime,especiallyfor3Dmodels.Tosimulatethin-walledstructures,structuralidealizationisoneoftheapproachestoreducecomputationtime.TheKirchhoff–Loveplate[3,4],theMindlin–Reissnerplate[5,6],andtheshell[7]modelshavebeenproposedinthePDliterature.Furthermore,severalengineeringapplicationsofthin-walledstructureshavebeenreportedconcerningnonlinearanalysis[8],buckling[9],vibration[10],stressintensityfactors[11,12],compositematerials[13,14],andshipstrength[15].

InCCM,crackopeningdisplacements(CODs),stressintensityfactors,andJ-integralarethemainfailurecriteriaindeterminingthestatusofcrackpropagationatthecracktip.WithinthePDframework,crackingisdictatedbythestatusofinteractionbondsbetweenmaterialpoints.Severalfailurecriteriathatconcerncriticalvaluesofinteractionbondscanbefoundinthepreviouspdstudies.SillingandAskari[16]introducedafailurecriterionbasedonbondelongation.Thisfailurecriterioniscalledthecriticalbondstretch.Becauseitonlyinvolvesthevolumetricdeformation,thiscriterionisinsensitivetothedeviatoricdeformationandmainlyappliestomode-Ifractureproblemsinbrittlematerials.Subsequently,twoenergy-basedfail-

ure criteria, called the critical energy density, were proposed in Refs. [17] and [18] to overcome underestimates in the critical bond stretch. Dipasquale and collaborators [19] examined the effectiveness of the failure criteria mentioned above in mixed-mode fracture problems. Moreover, COD [20], energy release rates [21], equivalent strain criterion [22], and the Johnson-Cook damage model [23] were introduced into the PD framework to predict fracture behaviors.

In computations, the PD surface effect originates from the assumption that the PD parameters are based on a complete horizon in the analysis domain. If the material points are located near domain boundaries or crack surfaces, the complete horizon assumption is not satisfied and therefore the accuracy of the computational results in BBPD and OSPD are strongly affected. Le and Bobaru [24] investigated 2D linear elastic and fracture problems with different surface effect corrections. In most surface effect corrections, the PD force density is corrected by multiplying correction factors to reduce the PD surface effect. The correction factors are obtained by comparing some physical quantities between the complete and incomplete horizons. Such correction methods only reduce the surface effect rather than eliminate it. The fictitious node method [25] can eliminate the surface effect in simple geometries. However, severe challenges are met in complex geometries, in particular, for configured models with cracks. An alternative approach to minimize the PD surface effect has been presented using arbitrary horizon domains. Queiruga and Moridis [26] performed a convergence analysis for three state-based PD models. In one of the PD models, the PD parameters were evaluated employing arbitrary horizon domains. Chen [27] presented a similar approach to calculate 2D static and dynamic problems. Madenci and collaborators proposed a state-based PD element in the finite element framework [28] and a weak form of the PD governing equations [29]. Using variable horizons, both proposed methods are free of the PD surface effect. 2D problems were only taken into account in the references mentioned above [26-29]. For the treatment of thin-walled structures using the arbitrary horizon domain method, out-of-plane deformations still have been not discussed.

The adopted OSPD shell model was examined previously for its capabilities in several areas of investigation [6,11,12,15]. For this reason, this PD model is employed in the present study to assess fracture mechanics behaviors of shell structures near crack surfaces subjected to in-plane or out-of-plane loading. Moreover, the arbitrary horizon domain method [26,27] is introduced into the PD framework to treat the PD surface effect. In the proposed

method, the membrane, bending, and transverse shear deformations are considered in computations of the PD parameters. To examine the effectiveness of the proposed method, CODs and strain energy densities (SEDs) that correspond respectively to the critical bond stretch [16] and critical energy density [17,18] criteria are investigated. Finally, a crack propagation analysis of a diagonally loaded square plate (DLSP) specimen [30] is analyzed.

The remainder of the paper is organized as follows. The PD shell model and numerical implementation are introduced in Section 2. The arbitrary horizon domain method for shell structures is presented in Section 3. Several numerical problems are demonstrated in Section 4. The conclusions are given in Section 5.

2. Ordinary state-based peridynamic theory

2.1. Peridynamic model for shell structures

The OSPD model for shell structures [6] is adopted in the present study. A schematic illustration of the PD shell model is presented in Fig. 1. $\boldsymbol{x}_{(k)}$ and $\boldsymbol{y}_{(k)}$ denote the initial and deformed positions of point k, respectively. φ represents the angle of the interaction bond between points k and j with respect to the x_1-axis, and h indicates the shell thickness. The set $\boldsymbol{u}_{(k)}$=$[u\ v\ w\ \theta_x\ \theta_y]^T$ denotes the displacement vector for six degrees of freedom. $\boldsymbol{t}_{(k)(j)}$ and $\boldsymbol{t}_{(j)(k)}$ represent the PD force density vectors between points k and j.

The PD SEDs are obtained by summing micro-potentials of all the material points within the specified area called the horizon, denoted H_x. The micro-potential depends on the bond stretch and constitutive properties of each interaction bond. For the OSPD shell model, the SEDs composed of the membrane, bending, and transverse shear terms are defined as follows:

$$\bar{W}^{PD}_{ip(k)} = a_{ip}\vartheta^2_{ip(k)} + b_{ip}\sum_{j=1}^{N}\underline{w}s^2_{ip(k)(j)}\xi^2 V_{(j)}, \tag{1}$$

$$\bar{W}^{PD}_{b(k)} = a_b\vartheta^2_{b(k)} + b_b\sum_{j=1}^{N}\underline{w}s^2_{b(k)(j)}\xi^2 V_{(j)}, \tag{2}$$

$$\bar{W}^{PD}_{s(k)} = \frac{1}{4}C_s\sum_{j=1}^{N}\underline{w}(\frac{w_{(j)}-w_{(k)}}{\xi} - \frac{\bar{\theta}_{(j)}+\bar{\theta}_{(k)}}{2})^2\xi^2 V_{(j)}, \tag{3}$$

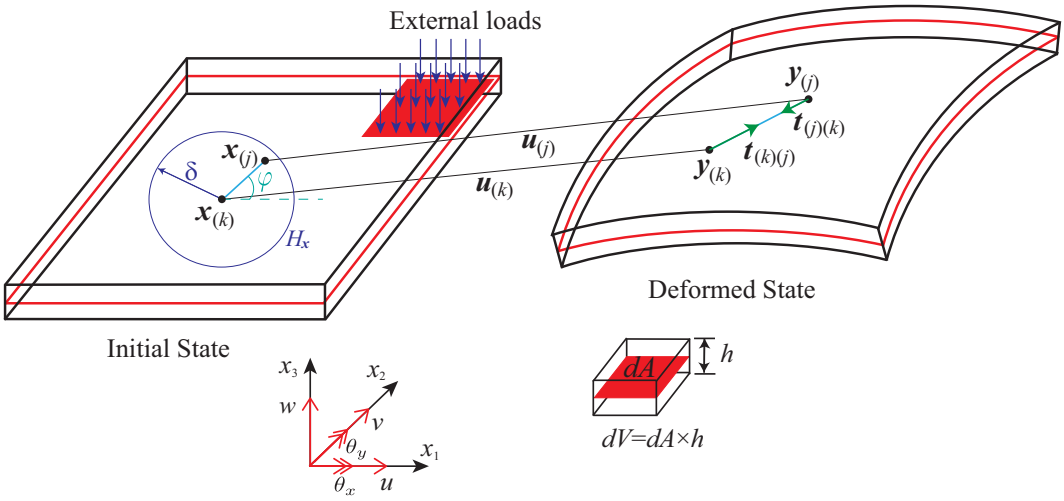

Figure 1: Initial and deformed states of a flat shell in PD.

where s, ϑ, and ξ denote the bond stretch, dilatation, and distance between $\boldsymbol{x}_{(k)}$ and $\boldsymbol{x}_{(j)}$, respectively. $\bar{\theta}_{(k)}$ and $\bar{\theta}_{(j)}$ represent the rotations of the interaction bond, and N indicates the total number of material points within H_x. The influence function is defined as $\underline{w}=\delta/\xi$, and a, b, d, and C denote the PD parameters. Subscripts ip, b, and s to the PD parameters signify that the quantities relate to the membrane, bending, and shear terms, respectively.

Bond stretch s is the relative deformation of the interaction bond, and dilatation ϑ is the relative variation in volume of the material point. Bond stretches s for the membrane and bending deformations are obtained from

$$s_{ip(k)(j)} = \frac{(u_{(j)} - u_{(k)})\cos\varphi + (v_{(j)} - v_{(k)})\sin\varphi}{\xi}, \tag{4}$$

$$s_{b(k)(j)} = \frac{-(\theta_{y(j)} - \theta_{y(k)})\cos\varphi + (\theta_{x(j)} - \theta_{x(k)})\sin\varphi}{\xi}. \tag{5}$$

Dilatations ϑ for the membrane and bending deformations are given by

$$\vartheta_{ip(k)} = d_{ip}\sum_{j=1}^{N} \underline{w} s_{ip(k)(j)} \xi V_{(j)}, \tag{6}$$

$$\vartheta_{b(k)} = d_b \sum_{j=1}^{N} \underline{w} s_{b(k)(j)} \xi V_{(j)}. \tag{7}$$

Rotations $\bar{\theta}_{(k)}$ and $\bar{\theta}_{(j)}$ with respect to the interaction bond between points k and j are defined as

$$\bar{\theta}_{(k)} = -\theta_{y(k)} \cos\varphi + \theta_{x(k)} \sin\varphi, \tag{8}$$

$$\bar{\theta}_{(j)} = -\theta_{y(j)} \cos\varphi + \theta_{x(j)} \sin\varphi. \tag{9}$$

The PD parameters are obtained by comparing dilatations and SEDs between CCM and PD. The PD parameters for the membrane, bending, and transverse shear terms are expressed as

$$a_{ip} = \frac{Eh(3\nu-1)}{4(1-\nu^2)}, \quad d_{ip} = \frac{3E}{\pi\delta^4(1+\nu)}, \quad b_{ip} = \frac{2}{\pi h\delta^3}, \tag{10}$$

$$a_b = \frac{Eh^3(3\nu-1)}{48(1-\nu^2)}, \quad d_b = \frac{Eh^2}{4\pi\delta^4(1+\nu)}, \quad b_b = \frac{2}{\pi h\delta^3}, \tag{11}$$

$$C_s = \frac{3k_sE}{\pi\delta^4(1+\nu)}, \tag{12}$$

where E, ν, k_s, and δ denote Young's modulus, Poisson's ratio, shear correction factor, and horizon size, respectively.

The potential energy is obtained from SEDs and work done by body forces. Substituting kinetic energy and potential energy into the Euler-Lagrange equation yields the PD equation of motion that is an integro-differential equation without spatial derivatives,

$$\begin{aligned} \boldsymbol{m}_{(k)}\ddot{\boldsymbol{u}}_{(k)} &= \int_{H_x} (\boldsymbol{t}_{(k)(j)} - \boldsymbol{t}_{(j)(k)}) V_{(j)} + \boldsymbol{b}_{(k)} \\ &= \int_{H_x} \boldsymbol{f}_{(k)(j)} V_{(j)} + \boldsymbol{b}_{(k)}, \end{aligned} \tag{13}$$

where $\boldsymbol{m}_{(k)}$, $\ddot{\boldsymbol{u}}_{(k)}$, and $\boldsymbol{b}_{(k)}$ denote the mass matrix, acceleration vector, and body force vector, respectively. $\boldsymbol{f}_{(k)(j)}$=$\boldsymbol{t}_{(k)(j)}$-$\boldsymbol{t}_{(j)(k)}$ represents the PD force density vector, and $V_{(j)}$ indicates the volume of point j. The PD equation of motion is briefly introduced here. Its derivation can be found in detail in Ref. [31]. Note that, in the proposed PD model, an assumption stipulating small deformations is imposed.

Material behavior exhibited in the PD framework is described by integrating nonlocal force interactions between material points. The nonlocal force densities are obtained from the derivation of the PD equation of motion. The PD force densities for each degree of freedom in the OSPD shell model are expressed as

$$f^{u}_{(k)(j)} = [2a_{ip}d_{ip}\underline{w}(\vartheta_{ip(k)} + \vartheta_{ip(j)}) + 4b_{ip}\underline{w}s_{ip(k)(j)}\xi]\cos\varphi, \tag{14}$$

$$f^{v}_{(k)(j)} = [2a_{ip}d_{ip}\underline{w}(\vartheta_{ip(k)} + \vartheta_{ip(j)}) + 4b_{ip}\underline{w}s_{ip(k)(j)}\xi]\sin\varphi, \tag{15}$$

$$\begin{aligned} f^{w}_{(k)(j)} =& C_s\underline{w}\{\frac{w_{(j)} - w_{(k)}}{\xi} - \frac{1}{2}[-(\theta_{y(k)} + \theta_{y(j)})\cos\varphi \\ &+ (\theta_{x(k)} + \theta_{x(j)})\sin\varphi]\}\xi, \end{aligned} \tag{16}$$

$$\begin{aligned} f^{\theta_x}_{(k)(j)} =& [2a_bd_b\underline{w}(\vartheta_{b(k)} + \vartheta_{b(j)}) + 4b_b\underline{w}s_{b(k)(j)}\xi]\sin\varphi \\ &+ \frac{1}{2}C_s\underline{w}\{(w_{(j)} - w_{(k)})\sin\varphi \\ &- \frac{\xi}{2}[-(\theta_{y(k)} + \theta_{y(j)})\sin\varphi\cos\varphi + (\theta_{x(k)} + \theta_{x(j)})\sin^2\varphi]\}\xi, \end{aligned} \tag{17}$$

$$\begin{aligned} f^{\theta_y}_{(k)(j)} =& -[2a_bd_b\underline{w}(\vartheta_{b(k)} + \vartheta_{b(j)}) + 4b_b\underline{w}s_{b(k)(j)}\xi]\cos\varphi \\ &- \frac{1}{2}C_s\underline{w}\{(w_{(j)} - w_{(k)})\cos\varphi \\ &- \frac{\xi}{2}[-(\theta_{y(k)} + \theta_{y(j)})\cos^2\varphi + (\theta_{x(k)} + \theta_{x(j)})\sin\varphi\cos\varphi]\}\xi. \end{aligned} \tag{18}$$

2.2. Surface effect correction and volume correction

Several numerical techniques are introduced within the PD shell framework to improve the accuracy of the computational results, including surface effect correction [24] and volume correction [31]. Meanwhile, the state of interaction bonds is also employed to model the crack segment. Therefore, the PD equation of motion is rewritten as

$$\boldsymbol{m}_{(k)}\ddot{\boldsymbol{u}}_{(k)} = \sum_{j=1}^{N} \mu_{(k)(j)} \lambda \boldsymbol{f}_{(k)(j)} \upsilon V_{(j)} + \boldsymbol{b}_{(k)}, \tag{19}$$

where $\mu_{(k)(j)}$ denotes the state of each interaction bond. λ and υ represent the correction factors for the surface effect and volume corrections, respectively. For static and quasi-static problems, the adaptive dynamic relaxation technique [31] is adopted in PD computations.

Although the volume method for the surface effect correction is based on the premise of homogeneous expansion, it is a simple and effective approach to reduce the surface effect in PD [24]. The volume method is chosen as one of the surface effect corrections in the present study. A schematic illustration of the volume method is shown in Fig. 2(a). The PD force density is revised in the volume method by multiplying a correction factor, λ, which is defined as the ratio of the complete volume to the present volume for the horizon; specifically,

$$\lambda = \frac{2V_0}{V_{(k)} + V_{(j)}}, \tag{20}$$

where $V_0{=}\pi\delta^2 h$ denotes the volume of the complete horizon, and $V_{(k)}$ and $V_{(j)}$ represent the volumes of the horizon at points k and j, respectively.

For nonlocal interactions between material points, the material point only possesses a partial volume near the horizon boundaries (see Fig. 2(b)). The blue and green regions signify that a material point possesses complete and partial volumes, respectively. The volume correction [31] is adopted to amend the volumes of the material points within the horizon. The volume correction factor υ is expressed as

$$\upsilon = \begin{cases} 1, & \xi < \delta - r, \\ (\delta + r - \xi)/2r, & \delta - r < \xi < \delta, \\ 0, & \delta < \xi, \end{cases} \tag{21}$$

where $r{=}\Delta x/2$ is defined.

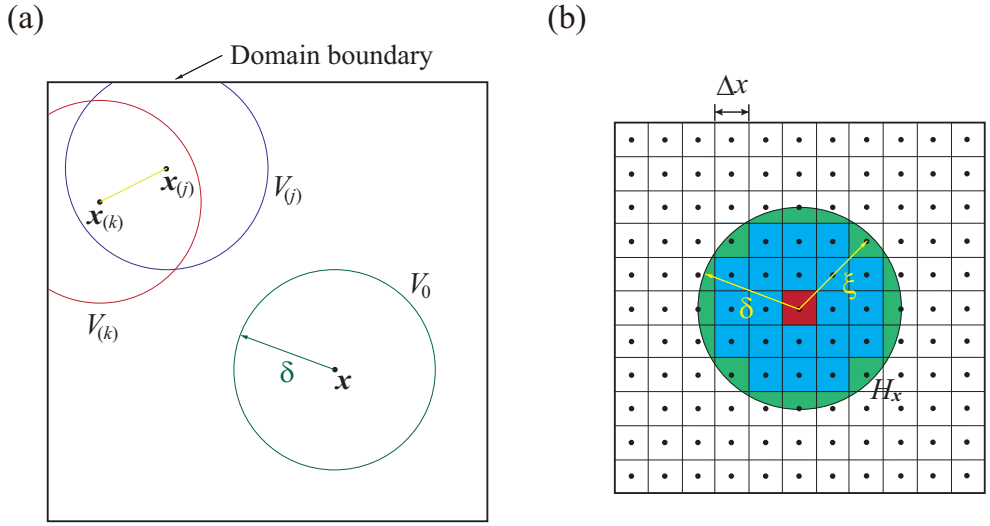

Figure 2: Surface effect correction and volume correction, (a) Volume method for surface effect correction, (b) Volume correction.

2.3. PD failure criteria

Here, the critical bond stretch [16] and critical energy density [17] criteria for interaction bonds are introduced. The critical bond stretch is the most popular failure criterion in the PD literature. The interaction bond between material points breaks when its bond stretch exceeds the critical value. The critical value is yielded from the total work required to eliminate all interactions across a newly created crack surface. The critical bond stretch in OSPD is expressed as

$$s_c = \sqrt{\frac{G_c}{(\frac{6}{\pi}\mu + \frac{16}{9\pi^2}(\kappa - 2\mu))\delta}}, \tag{22}$$

where G_c denotes the critical energy release rate, and μ and κ represent the shear modulus and bulk modulus, respectively.

If the time-dependent nonlinear phenomenon exhibits, such as elastic-plasticity or viscoplasticity, the critical bond stretch criterion is no longer applicable. To deal with rate-dependent plastic models, Foster and collaborators [18] proposed a failure criterion based on critical energy density in the PD framework. Subsequently, Madenci and Oterkus [17] presented an alternative energy-based criterion. For shell structures, an energy-based failure criterion was introduced in Ref. [6]. The critical value for each interaction bond g_c is computed by averaging the critical energy release rate; that is,

$$g_c = \frac{G_c}{N_c}, \tag{23}$$

where G_c denotes the critical energy release rate. N_c represents the total number of interaction bonds required to eliminate for creating a unit crack surface, with $N_c = 36$ for δ=3Δx [6].

The work done by PD force densities related to the energy release rate is regarded as a measure to determine the state of interaction bonds. The total energy density $\bar{g}_{(k)(j)}$ stored in each interaction bond is expressible as

$$\bar{g}_{(k)(j)} = \frac{1}{2\Delta x h}(\omega_{(k)(j)} + \omega_{(j)(k)})V_{(k)}V_{(j)}, \tag{24}$$

where Δx denotes the spacing of material points, and $\omega_{(k)(j)}$ and $\omega_{(j)(k)}$ represent the micro-potentials between points k and j.

The micro-potentials are obtained assuming linear elastic deformations. From the PD force densities acting on the deformed bond, the micro-potential $\omega_{(k)(j)}$ is determined from

$$\omega_{(k)(j)} = \frac{1}{2h}(t_{ip(k)(j)}s_{ip(k)(j)} + t_{b(k)(j)}s_{b(k)(j)} + t_{s(k)(j)}s_{s(k)(j)})\xi, \tag{25}$$

in which $s_{s(k)(j)}$=($w_{(j)}$-$w_{(k)}$)/ξ is defined.

The interaction bond is irreversibly broken between material points when the physical measure exceeds a critical value, either for the critical bond stretch or the critical energy density. The factor $\mu_{(k)(j)}$ is introduced into the PD equation of motion to denote the state of each interaction bond.

$$\mu_{(k)(j)} = \begin{cases} 0 & \text{broken bond,} \\ 1 & \text{intact bond.} \end{cases} \tag{26}$$

3. Arbitrary horizon domain method for PD parameters

In the regular approach to BBPD and OSPD, the PD parameters computed under a complete horizon are kept constant for every material point in the analysis domain. Because the horizon near domain boundaries or crack surfaces is incomplete, these constant PD parameters can not correctly reproduce material behavior (see Fig. 3). Therefore, several numerical corrections have been proposed to reduce the surface effect in BBPD and OSPD. To compensate for the difference in PD force densities near domain boundaries or crack surfaces, the force density is modified by multiplying a correction factor in most surface effect corrections. In contrast to regular surface effect corrections, the variable PD parameters are computed using the actual influence domain of the horizon in the arbitrary horizon domain method. The actual influence domains near discontinuities in the arbitrary horizon domain method are similar to the visibility criterion [32] in the meshfree method (see Fig. 4).

The arbitrary horizon domain method is introduced in this section. By comparing dilatations and SEDs between PD and CCM, the variable PD parameters are derived. In the OSPD shell model, the membrane, bending, and transverse shear deformations are included.

3.1. Membrane deformation

At first, the PD parameters in the membrane term are calculated. The displacement components of material point j are expressed using Taylor's series expansion,

$$\begin{aligned} u_{(j)} &= u_{(k)} + u_{,x(k)}(x_{(j)} - x_{(k)}) + u_{,y(k)}(y_{(j)} - y_{(k)}), \\ v_{(j)} &= v_{(k)} + v_{,x(k)}(x_{(j)} - x_{(k)}) + v_{,y(k)}(y_{(j)} - y_{(k)}), \end{aligned} \tag{27}$$

which can be rewritten as

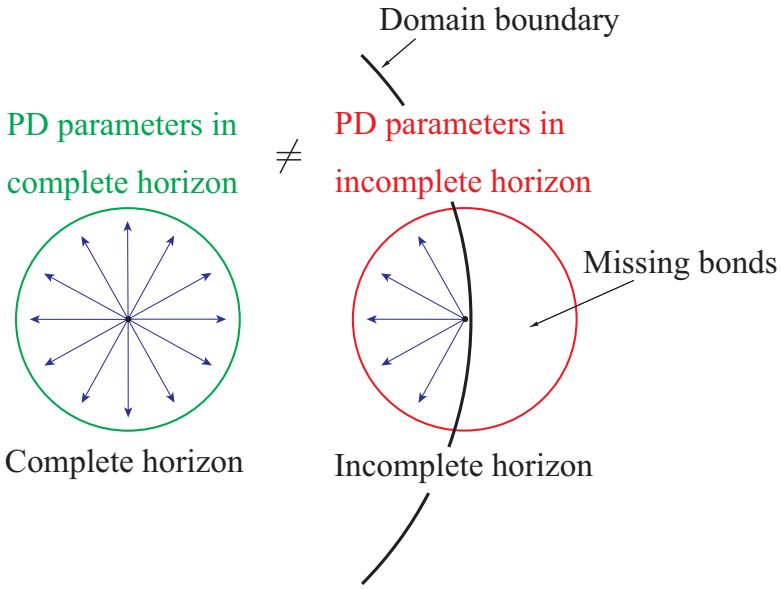

Figure 3: Surface effect in PD caused from PD parameters computation.

$$\begin{aligned} \frac{u_{(j)} - u_{(k)}}{\xi} &= u_{,x(k)} \cos\varphi + u_{,y(k)} \sin\varphi, \\ \frac{v_{(j)} - v_{(k)}}{\xi} &= v_{,x(k)} \cos\varphi + v_{,y(k)} \sin\varphi. \end{aligned} \tag{28}$$

Substituting Eq. (28) into Eq. (4) yields an expression of the bond stretch for the membrane term

$$s_{ip(k)(j)} = u_{,x(k)} \cos^2\varphi + u_{,y(k)} \sin\varphi\cos\varphi + v_{,x(k)} \sin\varphi\cos\varphi + v_{,y(k)} \sin^2\varphi. \tag{29}$$

Under the isotropic expansion condition ($u_{,x(k)}$=ζ, $v_{,y(k)}$=ζ), the dilatation of PD in Eq. (6) becomes

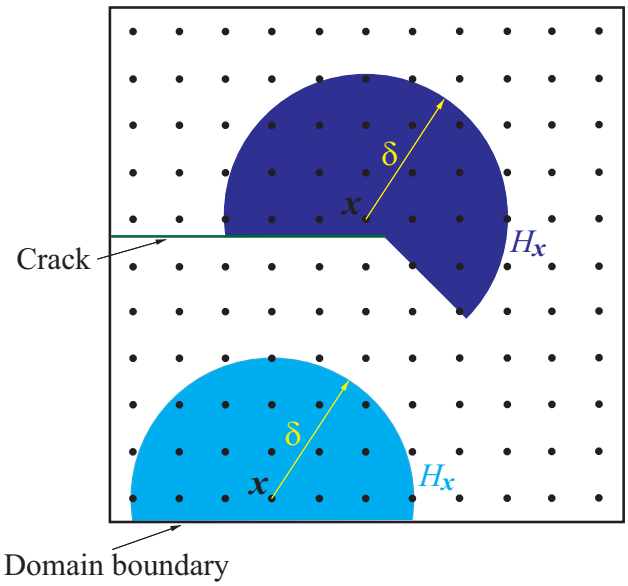

Figure 4: Actual influence domain of the horizon near a domain boundary and a crack surface.

$$\begin{aligned}\vartheta_{ip(k)}^{PD} =& d_{ip}h\int_{H_x}\underline{w}s_{ip(k)(j)}\xi dA\\ =& d_{ip}h\int_{H_x}\underline{w}(\zeta\cos^2\varphi+\zeta\sin^2\varphi)\xi dA\\ =& d_{ip}h\int_{H_x}\underline{w}\zeta\xi dA.\end{aligned}\tag{30}$$

The dilatation of CCM under the isotropic expansion condition becomes

$$\vartheta_{ip(k)}^{CM}=2\zeta.\tag{31}$$

By comparing the dilatation for the membrane term between PD and CCM, the PD parameter d_{ip} is obtained,

$$d_{ip}=\frac{2}{h\int_{H_x}\underline{w}\xi dA}.\tag{32}$$

Similarly, the SED of PD in Eq. (1) under the isotropic expansion condition ($u_{,x(k)}$=ζ, $v_{,y(k)}$=ζ, and $\vartheta_{ip(k)}$=2ζ) becomes

$$\begin{aligned}\bar{W}_{ip}^{PD} =& a_{ip}\vartheta_{ip(k)}^2+b_{ip}h\int_{H_x}\underline{w}s_{ip(k)(j)}^2\xi^2dA\\ =& a_{ip}(2\zeta)^2+b_{ip}h\int_{H_x}\underline{w}\zeta^2\xi^2dA.\end{aligned}\tag{33}$$

The SED of CCM under the isotropic expansion condition becomes

$$\bar{W}_{ip(k)}^{CM}=\frac{Eh}{1-\nu}\zeta^2.\tag{34}$$

By comparing the SED for the membrane term between PD and CCM, the PD parameter a_{ip} is obtained,

$$a_{ip}=\frac{E}{4(1-\nu)}-\frac{b_{ip}h}{4}\int_{H_x}\underline{w}\xi^2dA.\tag{35}$$

Under the simple shear condition ($u_{,y(k)}$=ζ, $v_{,x(k)}$=ζ, and $\vartheta_{ip(k)}$=0), the SED of PD in Eq. (1) becomes

$$\begin{aligned}\bar{W}_{ip}^{PD} =& b_{ip}h\int_{H_x}\underline{w}s_{ip(k)(j)}^{2}\xi^{2}dA\\ =& b_{ip}h\int_{H_x}\underline{w}(\zeta\sin\varphi\cos\varphi)^{2}\xi^{2}dA.\end{aligned} \tag{36}$$

The SED of CCM under the simple shear condition becomes

$$\bar{W}_{ip(k)}^{CM}=\frac{Eh}{4(1+\nu)}\zeta^{2}. \tag{37}$$

In a similar comparison of the SED, the PD parameter b_{ip} is obtained,

$$b_{ip}=\frac{E}{4(1+\nu)}\frac{1}{\int_{H_x}\underline{w}(\xi\cos\varphi\sin\varphi)^{2}dA}. \tag{38}$$

3.2. Bending deformation

Next, the PD parameters in the bending term are calculated in a similar manner to the computation of the membrane term. Using Taylor series expansion, the rotation components of material point j are expressed,

$$\begin{aligned}\theta_{x(j)}&=\theta_{x(k)}+\theta_{x,x(k)}(x_{(j)}-x_{(k)})+\theta_{x,y(k)}(y_{(j)}-y_{(k)}),\\ \theta_{y(j)}&=\theta_{y(k)}+\theta_{y,x(k)}(x_{(j)}-x_{(k)})+\theta_{y,y(k)}(y_{(j)}-y_{(k)}),\end{aligned} \tag{39}$$

which can be rewritten as

$$\begin{aligned}\frac{\theta_{x(j)}-\theta_{x(k)}}{\xi}&=\theta_{x,x(k)}\cos\varphi+\theta_{x,y(k)}\sin\varphi,\\ \frac{\theta_{y(j)}-\theta_{y(k)}}{\xi}&=\theta_{y,x(k)}\cos\varphi+\theta_{y,y(k)}\sin\varphi.\end{aligned} \tag{40}$$

By substituting Eq. (40) into Eq. (5), the bond stretch for the bending term is expressed as

$$s_{b(k)(j)} = -\theta_{y,x(k)} \cos^2 \varphi - \theta_{y,y(k)} \sin \varphi \cos \varphi + \theta_{x,x(k)} \sin \varphi \cos \varphi + \theta_{x,y(k)} \sin^2 \varphi. \tag{41}$$

Under the isotropic rotation condition ($-\theta_{y,x(k)}$=ζ, $\theta_{x,y(k)}$=ζ), the dilatation of PD in Eq. (7) becomes

$$\begin{aligned} \vartheta_{b(k)}^{PD} =& d_b h \int_{H_x} \underline{w} s_{b(k)(j)} \xi dA \\ =& d_b h \int_{H_x} \underline{w} (\zeta \cos^2 \varphi + \zeta \sin^2 \varphi) \xi dA \\ =& d_b h \int_{H_x} \underline{w} \zeta \xi dA. \end{aligned} \tag{42}$$

The dilatation of CCM under the isotropic rotation condition becomes

$$\vartheta_{b(k)}^{CM} = 2\zeta. \tag{43}$$

By comparing the dilatation for the bending term between PD and CCM, the PD parameter d_b is obtained,

$$d_b = \frac{2}{h \int_{H_x} \underline{w} \xi dA}. \tag{44}$$

Similarly, the SED of PD in Eq. (2) under the isotropic rotation condition ($-\theta_{y,x(k)}$=ζ, $\theta_{x,y(k)}$=ζ, and $\vartheta_{b(k)}$=2ζ) becomes

$$\begin{aligned} \bar{W}_b^{PD} =& a_b \vartheta_{b(k)}^2 + b_b h \int_{H_x} \underline{w} s_{b(k)(j)}^2 \xi^2 dA \\ =& a_b (2\zeta)^2 + b_b h \int_{H_x} \underline{w} \zeta^2 \xi^2 dA. \end{aligned} \tag{45}$$

The SED of CCM under the isotropic rotation condition becomes

$$\bar{W}_{b(k)}^{CM} = \frac{E h^3}{12(1-\nu)} \zeta^2. \tag{46}$$

By comparing the SED for the bending term between PD and CCM, the PD parameter a_b is obtained,

$$a_b = \frac{Eh^3}{48(1-\nu)} - \frac{b_b h}{4}\int_{H_x} \underline{w}\xi^2 dA. \tag{47}$$

Under the torsion condition ($-\theta_{y,y(k)}=\zeta$, $\theta_{x,x(k)}=\zeta$, and $\vartheta_{b(k)}=0$), the SED of PD in Eq. (2) becomes

$$\begin{aligned}\bar{W}_b^{PD} =& b_b h \int_{H_x} \underline{w} s_{b(k)(j)}^2 \xi^2 dA \\ =& b_b h \int_{H_x} \underline{w}(\zeta \sin\varphi\cos\varphi)^2 \xi^2 dA.\end{aligned} \tag{48}$$

The SED of CCM under the torsion condition becomes

$$\bar{W}_{b(k)}^{CM} = \frac{Eh^3}{48(1+\nu)}\zeta^2. \tag{49}$$

In a similar comparison of the SED, the PD parameter b_b is obtained,

$$b_b = \frac{Eh^2}{48(1+\nu)} \frac{1}{\int_{H_x} \underline{w}(\xi\cos\varphi\sin\varphi)^2 dA}. \tag{50}$$

3.3. Transverse shear deformation

Finally, the PD parameter in the transverse shear term is calculated. The transverse displacement component of material point j is expressed using Taylor's series expansion,

$$w_{(j)} = w_{(k)} + w_{,x(k)}(x_{(j)} - x_{(k)}) + w_{,y(k)}(y_{(j)} - y_{(k)}), \tag{51}$$

which can be rewritten as

$$\frac{w_{(j)} - w_{(k)}}{\xi} = w_{,x(k)}\cos\varphi + w_{,y(k)}\sin\varphi. \tag{52}$$

By substituting Eq. (52) into Eq. (3) and assuming $\bar{\theta}_{(k)}$=$\bar{\theta}_{(j)}$, the SED of PD under the transverse shear deformation (($w_{,x}$+θ_y)=ζ, ($w_{,y}$-θ_x)=ζ) becomes

$$\begin{aligned}\bar{W}_s^{PD} =&\frac{1}{4}C_s h\int_{H_x}\underline{w}(\frac{w_{(j)}-w_{(k)}}{\xi}-\bar{\theta}_{(k)})^2\xi^2 dA\\ =&\frac{1}{4}C_s h\int_{H_x}\underline{w}[(w_{,x}+\theta_y)\cos\varphi+(w_{,y}-\theta_x)\sin\varphi]^2\xi^2 dA\\ =&\frac{1}{4}C_s h\int_{H_x}\underline{w}(\zeta^2\cos^2\varphi+\zeta^2\sin^2\varphi)\xi^2 dA\\ =&\frac{1}{4}C_s h\int_{H_x}\underline{w}\zeta^2\xi^2 dA.\end{aligned} \tag{53}$$

The SED of CCM under the transverse shear deformation becomes

$$\bar{W}_s^{CM}=\frac{k_s E h}{2(1+\nu)}\zeta^2. \tag{54}$$

By comparing the SED for the transverse shear term between PD and CCM, the PD parameter C_s is obtained,

$$C_s=\frac{k_s E}{1+\nu}\frac{2}{\int_{H_x}\underline{w}\xi^2 dA}. \tag{55}$$

For the proposed method, the PD parameters integrated over the complete circle horizon are the same as those given in the regular approach [6]. It confirms that the PD parameters are correctly derived in the arbitrary horizon domain method. In the computational procedure, the PD parameters are numerically integrated by summing the integrand over the horizon. The volume correction is thereby also adopted into the numerical integration of the PD parameters.

4. Numerical examples

The arbitrary horizon domain method incorporated with the OSPD shell model is employed in the present study. Four numerical examples of shell

structures are considered to examine fracture mechanics behaviors under in-plane or out-of-plane loading. CODs and SEDs corresponding to the critical bond stretch and critical energy density criteria, respectively, are regarded as the assessed objectives. Additionally, a crack propagation analysis is also performed using the proposed method. A uniform particle distribution is employed and the horizon size δ is set to $3.015\Delta x$ [31] in the numerical examples; here, Δx denotes the particle spacing.

Three PD approaches are considered in this study. Those approaches are labeled "Approach 1" for the regular method without correction, "Approach 2" for the volume method, and "Approach 3" for the arbitrary horizon domain method. The volume correction mentioned in Eq. (21) is adopted in all three approaches. A commercial FEM software, ABAQUS [34], is used to compute reference results with linear elastic fracture mechanics settings. The element size of the FEM models near the crack tip is set to approximately 0.001 m.

4.1. 2D plane stress problem for the near-tip solution with a stationary crack under Mode-I fracture

An infinite plate including a central crack under biaxial tensile load is analyzed. To simplify this example, a 2D plane stress model under specified displacement boundary conditions (BCs) is considered to examine near-tip fracture behaviors in linear elastic fracture mechanics. The length L and width W are set to 1 m, and the crack length a is set to 0.5 m. E=1 GPa and ν=0.25 are chosen for the material properties. From the model for this analysis in Fig. 5, the analytical solutions for the displacement and stress fields [33] are expressed in the form

$$\begin{bmatrix} u \\ v \end{bmatrix} = \frac{K_I}{2\mu}\sqrt{\frac{r'}{2\pi}} \begin{bmatrix} \cos\frac{\theta'}{2}(\kappa - 1 + 2\sin^2\frac{\theta'}{2}) \\ \sin\frac{\theta'}{2}(\kappa + 1 - 2\cos^2\frac{\theta'}{2}) \end{bmatrix}, \tag{56}$$

$$\begin{bmatrix} \sigma_{xx} \\ \sigma_{yy} \\ \tau_{xy} \end{bmatrix} = \frac{K_I}{\sqrt{2\pi r}} \begin{bmatrix} \cos\frac{\theta'}{2}(1 - \sin\frac{\theta'}{2}\sin\frac{3\theta'}{2}) \\ \cos\frac{\theta'}{2}(1 + \sin\frac{\theta'}{2}\sin\frac{3\theta'}{2}) \\ \cos\frac{\theta'}{2}\sin\frac{\theta'}{2}\cos\frac{3\theta'}{2} \end{bmatrix}, \tag{57}$$

where μ=E/2(1+ν) and κ=(3-ν)/(1+ν). K_I=1.0 MPa$\sqrt{\text{mm}}$ is set. The origin for the polar coordinate system (r',θ') is placed at the crack tip. Specified displacement BCs given in Eq. (56) are applied within the green region.

Three different particle spacings are used, specifically, Δx=1/80, 1/160, and 1/320 m.

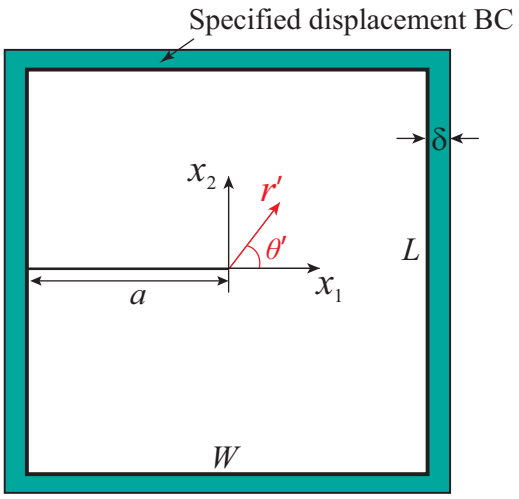

Figure 5: 2D plane stress model under specified displacement BCs with a stationary crack.

A convergence analysis of the displacement fields is performed. The L2-norm in Eq. (58) is selected to estimate the error by comparing the PD results with the analytical solution. The rates of convergence for the entire domain and the crack surface are presented in Fig. 6(a) and (b), respectively. Approach 1 produces slower convergence rates in both circumstances. Similar convergence rates in Fig. 6(a) are found for Approaches 2 and 3. In Fig. 6(b), however, Approach 3 has a better convergence rate than Approach 2.

$$error = \sqrt{\int_{\Omega} (u^{PD} - u^{Ref})^2 d\Omega}, \tag{58}$$

where u^{PD} and u^{Ref} are the displacement results from the PD and reference solutions, respectively.

The COD results, u_y, obtained from the analytical solution and Approach 3 are compared along the crack surface (see Fig. 7(a)). Both sets of results are in good agreement with each other. Furthermore, the SED along the crack surface and crack front is investigated. The SED results of the analytical solution and three PD approaches are illustrated in Fig. 7(b). The SED

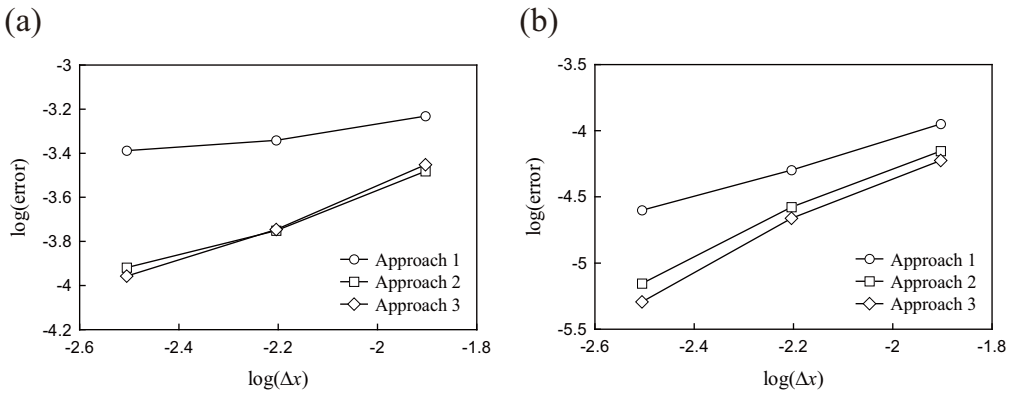

Figure 6: Convergence analysis of the displacement fields, (a) Entire domain, (b) Crack surface.

results of Approach 3 are found to be most similar to those of the analytical solution. Moreover, the arbitrary horizon domain method is able to evaluate the SED in linear elastic fracture mechanics. Even near the crack tip, the proposed method provides a reasonable SED solution.

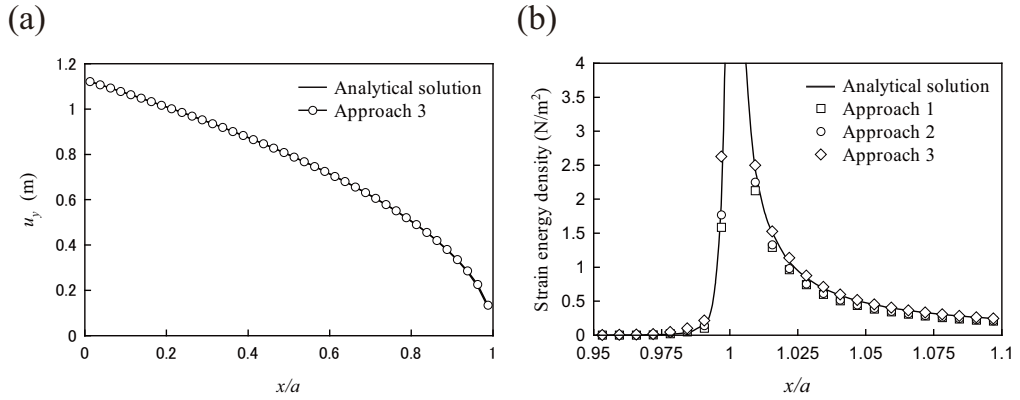

Figure 7: Fracture mechanics quantities, (a) Displacement u_y, (b) Strain energy density.

4.2. Rectangular shell with an inclined edge crack under tensile load

A rectangular shell including an inclined edge crack under tensile load is calculated. The length L, width W, and thickness h of the rectangular shell are 1 m, 0.5 m, and 0.1 m, respectively. The crack length a is 0.2 m, and the crack angle β is 45°. A uniform tensile stress of σ=1.0 MPa is applied to the top edge, and displacement BCs are adopted on the bottom edge (see Fig. 8). Young's modulus E and Poisson's ratio ν are set to 200 GPa and 0.3, respectively. A particle spacing of Δx=1/320 m is used.

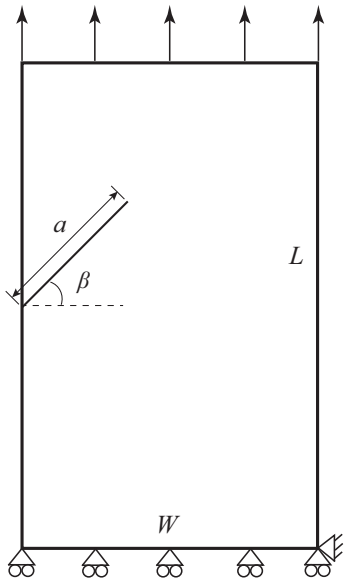

Figure 8: Rectangular shell under tensile load with an inclined edge crack.

The COD results, u_y, along the inclined crack surface are presented in Fig. 9(a). Approach 3 appears to match well with the FEM solution than the other two approaches. The deformation contours, u_y, from Approach 3 and FEM are given in Fig. 10. From linear elastic fracture mechanics, the stresses tend to infinity near the crack tip. Because of the stress singularity, the near-tip stress fields can not be determined from FEM simulations. Therefore, a comparison of the SED results is plotted (see Fig. 9(b)) from x'/a=1.1 along the crack front; here, x' denotes the x-axis of the local Cartesian coordinate system. From this comparison, the SED results of Approach 1 show an obvious difference from those of Approaches 2 and 3. After further

discussion, the SED results of Approach 2 are slightly lower than those of the FEM solution, and Approach 3 provides the closest SED results to the FEM solution. It indicates that the arbitrary horizon domain method well assesses COD and SED for mixed-mode fracture problems.

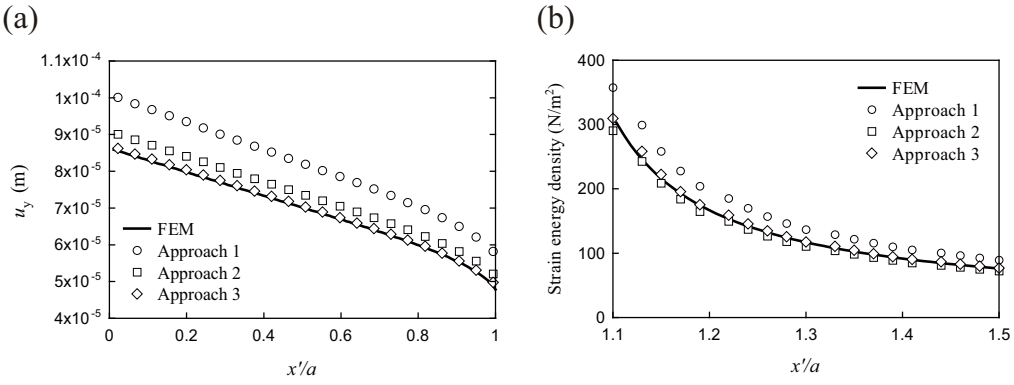

Figure 9: Fracture mechanics quantities, (a) Displacement u_y, (b) Membrane strain energy density.

4.3. Square shell with a central crack under uniform pressure

A square shell including a central crack under uniform pressure is investigated. The geometrical dimensions of the shell are L=W=1 m and h=0.1 m. The half crack length a=0.1 m is adopted. The shell is subjected to a uniform pressure of p_0=1.0 MPa in the transverse direction with clamped BCs imposed on all the edges (see Fig. 11). E=200 GPa and ν=0.3 are chosen for the material properties. A particle spacing of Δx=1/320 m is used.

The COD results, including u_z, θ_x, and θ_y, along the crack surface are shown in Fig. 12(a), (b), and (c), respectively. The COD results are improved under Approach 3 to obtain the most similar results to the FEM solution for not only transverse deformation but also rotation deformations. The deformation contours, θ_x, from Approach 3 and FEM are presented in Fig. 13. The SED of the bending term dominates in the example instead of the transverse shear term. Therefore, only the SED of the bending term illustrated in Fig. 12(d) is discussed. The SED results of both Approaches 2 and 3 agree well with those of the FEM solution. In general, accurate

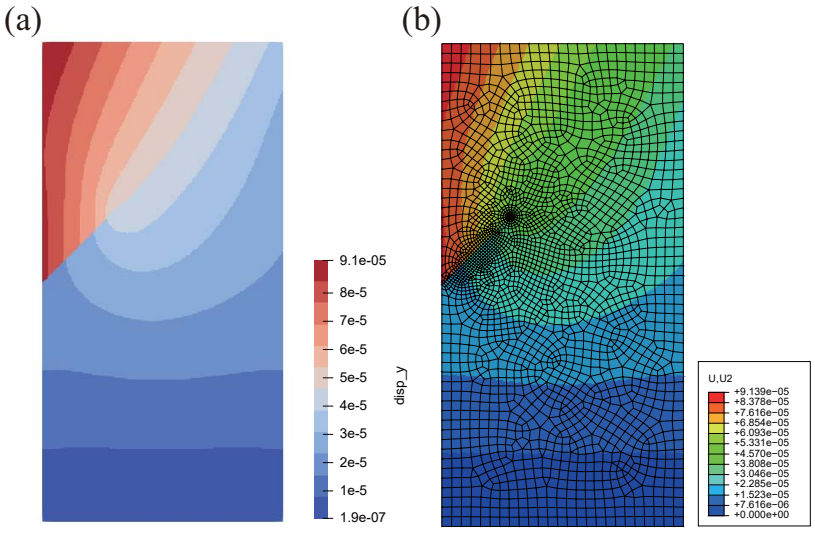

Figure 10: u_y deformation contours, (a) Approach 3, (b) FEM.

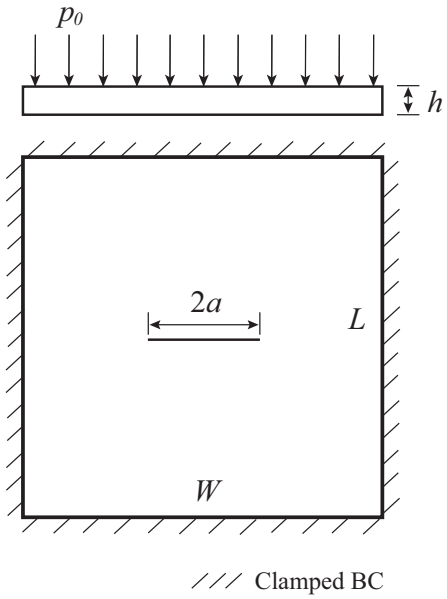

Figure 11: Square shell under uniform pressure with a central crack.

results for CODs and SED under out-of-plane loading can be obtained from the arbitrary horizon domain method.

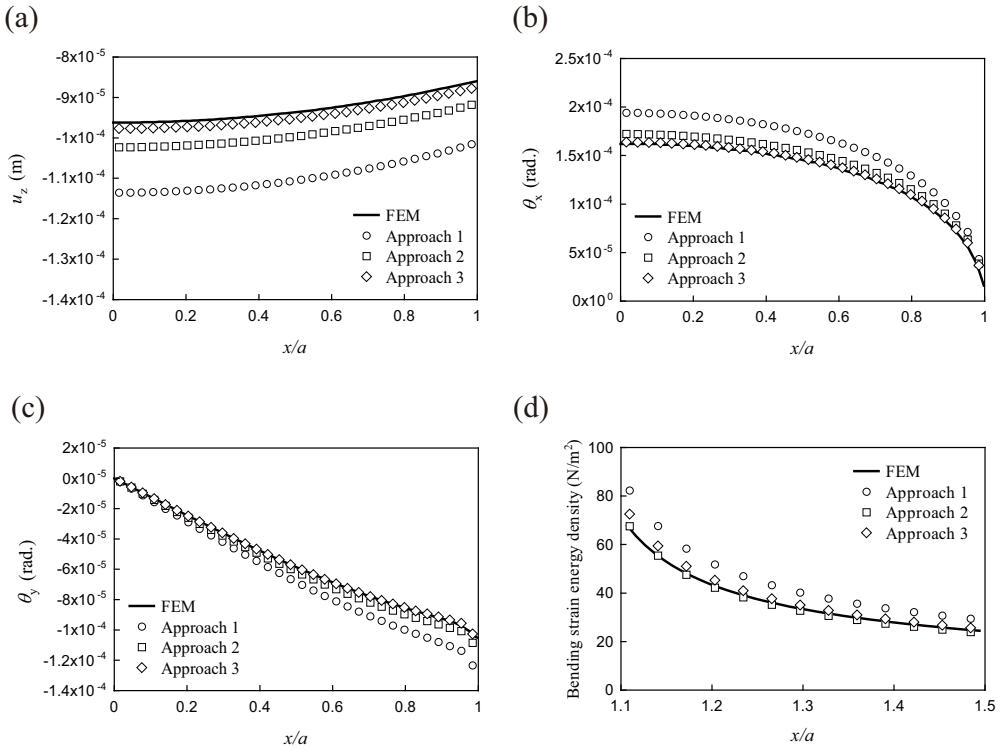

Figure 12: Fracture mechanics quantities, (a) Displacement u_z, (b) Rotation θ_x, (c) Rotation θ_y, (d) Bending strain energy density.

4.4. Rectangular shell with an inclined central crack under bending load

A rectangular shell including an inclined central crack under bending load is simulated. The length L=0.5 m, width W=1.0 m, and thickness h=0.1 m are set. The half crack length a and crack angle β are 0.1 m and 45°, respectively. The rectangular shell is subjected to bending moments of M=10.0 kPa-m with simply supported BCs along the right and left edges (see Fig. 14). Young's modulus E and Poisson's ratio ν are set to 200 GPa and 0.3, respectively, and a particle spacing of Δx=1/320 m is used.

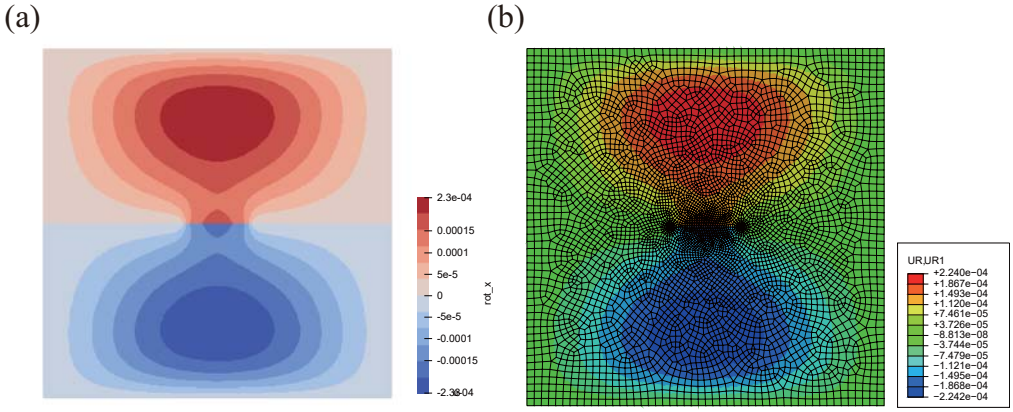

Figure 13: θ_x deformation contours, (a) Approach 3, (b) FEM.

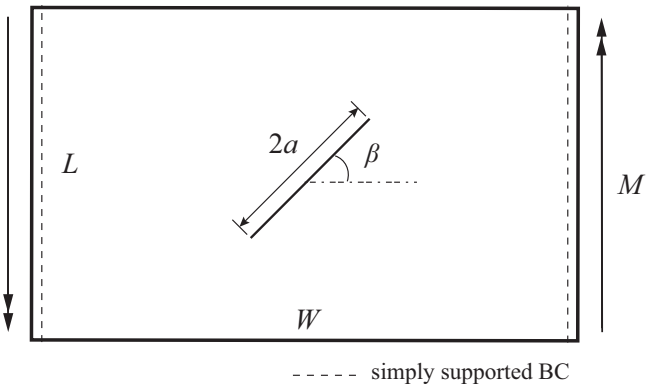

Figure 14: Rectangular shell under bending load with an inclined central crack.

The COD results for u_z, θ_x, and θ_y along the inclined crack surface are presented in Fig. 15(a), (b), and-(c), respectively. As for the third example, the results for the transverse and rotation deformations from Approach 3 are most similar to those from the FEM solution. The deformation contours, θ_y, from Approach 3 and FEM are drawn in Fig. 16. Likewise, a comparison of the SED results of the bending term along the crack front from x'/a=1.1 is plotted in Fig. 15(d). In contrast to Approach 1, Approaches 2 and 3 distinctly provide better SED results. In a detailed comparison between Approaches 2 and 3, the SED results of Approach 3 are closest to those of the FEM solution. In other words, CODs and SED in mixed-mode fracture problems involving out-of-plane loading are well reproduced using the arbitrary horizon domain method.

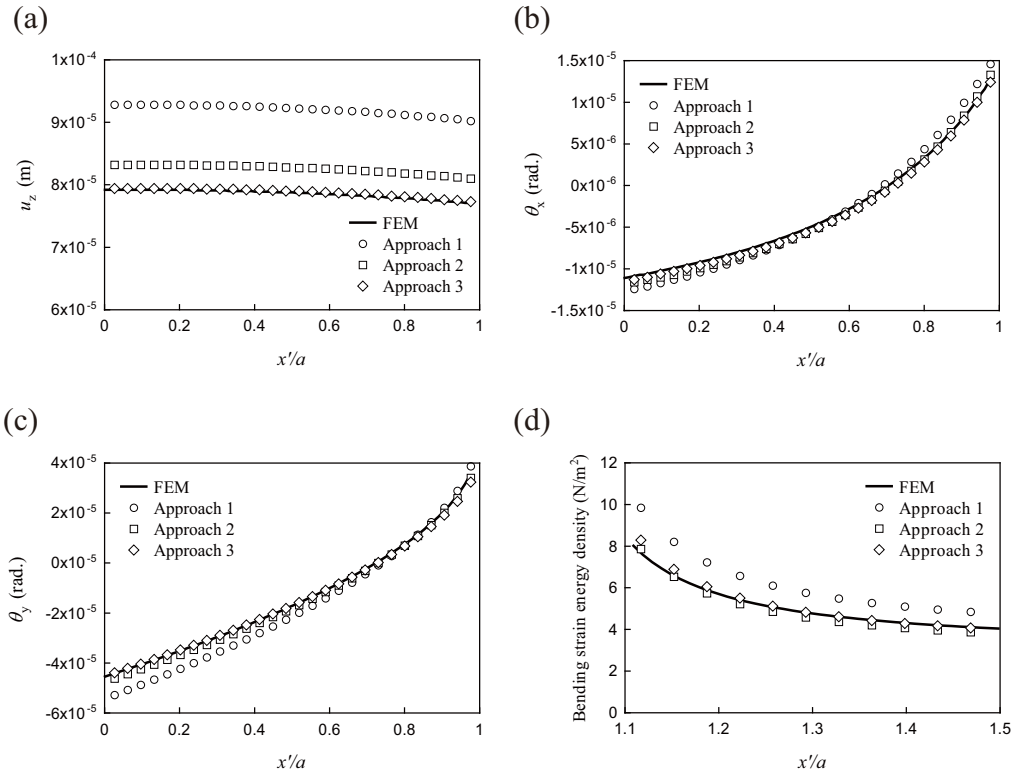

Figure 15: Fracture mechanics quantities, (a) Displacement u_z, (b) Rotation θ_x, (c) Rotation θ_y, (d) Bending strain energy density.

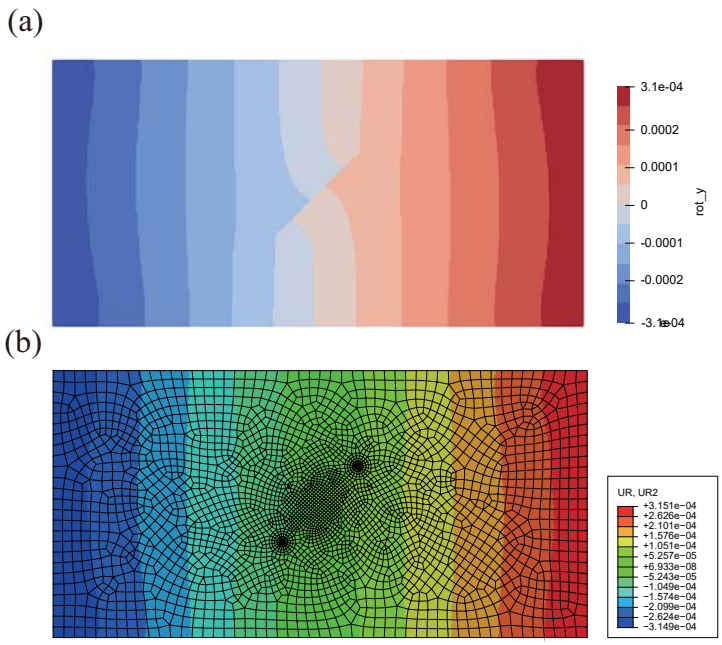

Figure 16: θ_y deformation contours, (a) Approach 3, (b) FEM.

4.5. Diagonally loaded square plate with a central pre-existing crack

A crack propagation analysis of the DLSP specimen [30] with an inclined central crack is performed. The geometrical dimension $2W$ and shell thickness h are 0.15 m and 0.005 m, respectively. The initial half crack length a is set to 0.045, and the crack orientation β is set to one of five values, specifically, 0°, 15°, 30°, 45°, and 62.5°. Young's modulus E=2.94 GPa, Poisson's ratio ν=0.38, and density ρ=1,200 kg/m^3 are chosen. A constant displacement increment Δu=2.5$\times$ 10^{-7} m [35] is applied within the hole regions at the top and bottom corners. The radius of each hole region is 0.004 m, and the distance q between the center of each hole region and the plate corner is 0.025 m. The DLSP model for this analysis is sketched in Fig. 17. A particle spacing of Δx=0.001 m is used. The fracture toughness of this material K_c is set at 1.33 MPa$\sqrt{\text{m}}$, and its critical energy release rate G_c is set at 601.667 N/m. The critical bond stretch s_c obtained from Eq. (22) is 9.145$\times$ 10^{-3}.

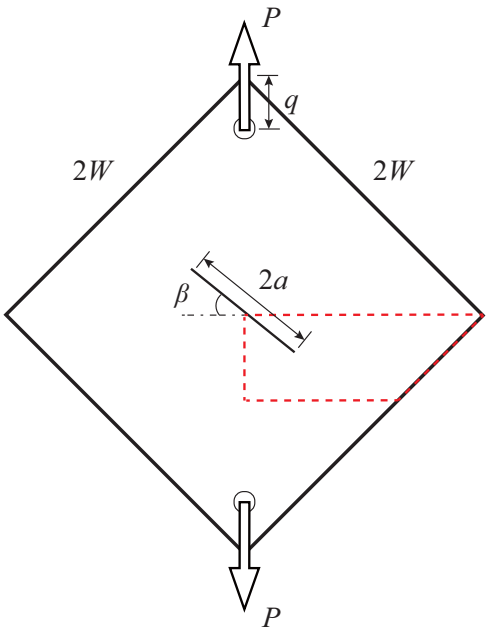

Figure 17: Diagonally loaded square plate with a central pre-existing crack.

The material of the DLSP specimen is a brittle polymer called polymethyl methacrylate (PMMA). From the numerical examples above, CODs are well

evaluated near the crack tip under single- and mixed-mode fracture conditions. Moreover, SEDs can not be correctly predicted near the crack tip because of the stress singularity. Therefore, a critical bond stretch criterion which is suited for brittle materials is adopted. Additionally, Approach 3 is employed in this crack propagation analysis.

The crack propagation paths for different crack orientations obtained from PD and experiment [30] are presented in Fig. 18. To examine the crack paths in detail, crack path comparisons with initial crack orientations 15° to 62.5° within the region marked by red dashed lines in the model are shown in Fig. 19. The reference solutions from experiment and extended FEM [36] are selected. From the comparisons, the crack paths are well predicted for all crack orientations when using the arbitrary horizon domain method. Moreover, the initial crack growth angle for different crack orientations is investigated in a comparison of PD and experiment. As expressed in Fig. 20, the PD results are in good agreement with those from experimental data.

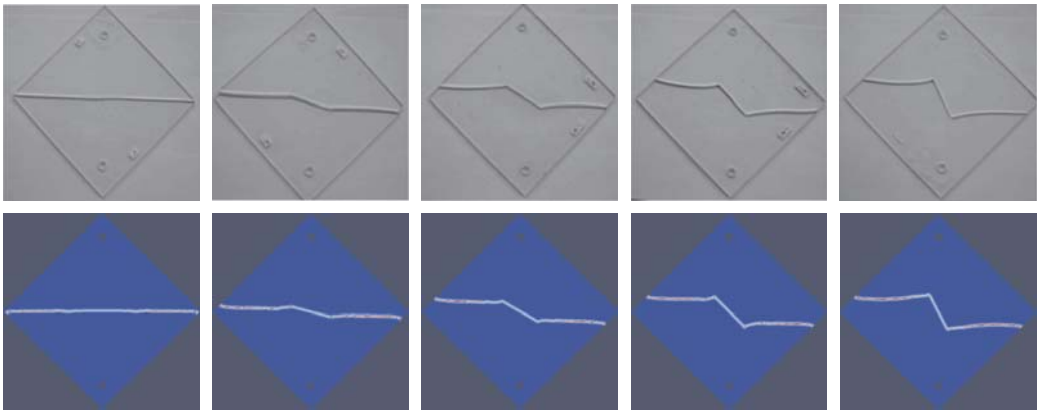

Figure 18: Crack propagation paths from experiment [30] (upper) and PD (lower).

5. Conclusion

The OSPD shell model is introduced to evaluate fracture mechanics behaviors of thin-walled structures. In the PD framework, the surface effect takes place near domain boundaries or crack surfaces because the PD parameters concerning the complete horizon assumption are constant. The restriction significantly affects the accuracy of computations. The arbitrary

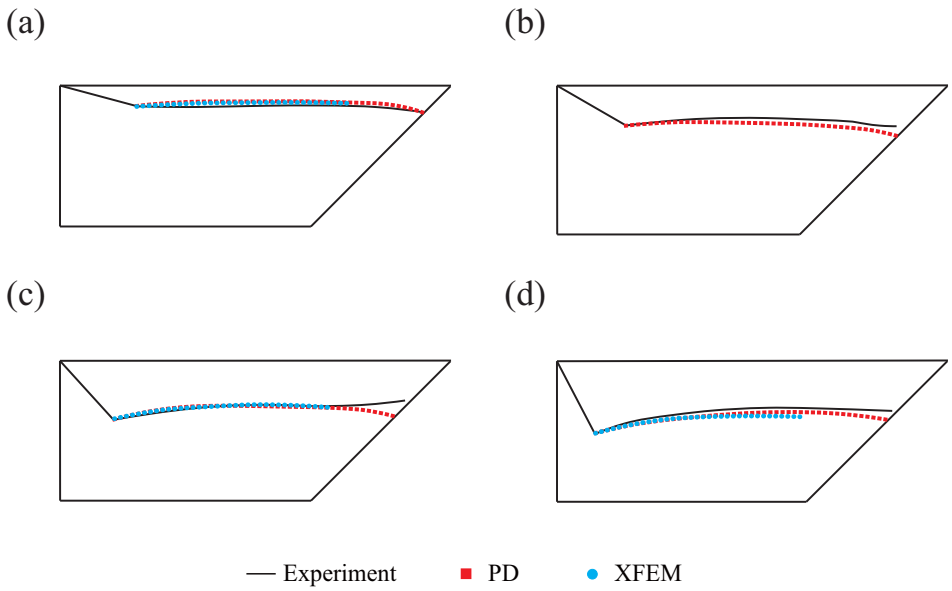

Figure 19: Detailed comparison of crack propagation paths between experiment, PD, and extended FEM [36].

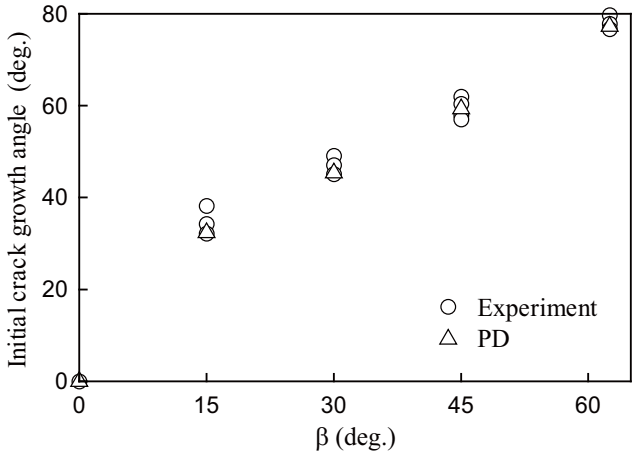

Figure 20: Initial crack growth angles from experiment and PD.

horizon domain method is adopted to reduce the PD surface effect by eliminating the complete horizon assumption. Only two-dimensional scenarios, however, have been considered in previous studies. Here, the arbitrary horizon domain method regraded as a surface effect correction is incorporated into the OSPD shell model to amend the PD parameters, including the membrane, bending, and transverse shear terms. Moreover, the volume correction and adaptive dynamic relaxation techniques are employed into this proposed framework.

Several numerical examples are considered to examine CODs and SEDs under in-plane or out-of-plane loading. Single- and mixed-mode fracture problems are included in those numerical examples. The COD and SED results obtained from three different PD approaches are compared with those from FEM simulations. The volume method and the arbitrary horizon domain method provide effective approaches to decrease the influence of the PD surface effect. Both methods consider the actual volume of the horizon for each material point in the analysis domain. However, the volume method assumes that each material bond within the horizon contributes equally to the PD force density. Thus, the PD force density is approximated by merely multiplying a ratio of the complete volume to the present volume when the horizon is located near domain boundaries or crack surfaces. In contrast to the volume method, as expounded in Section 3, the PD parameters in the arbitrary horizon domain method are functions of distance and angle between material points. For the PD force density, each material bond within the horizon no longer contributes equally. The arbitrary horizon domain method can precisely simulate physical behaviors near domain boundaries or crack surfaces than the volume method. From the comparisons presented in Section 4, the arbitrary horizon domain method shows good agreement with the FEM solution better than the other two approaches. Moreover, the proposed method is applied to predict crack paths in the crack propagation analysis of the DLSP specimen. These predictions for different crack orientations well-matched the data from experiment.

Appendix A. Examination of varied plate thickness

To verify the capability of the arbitrary horizon domain method for shells with different thicknesses, the same example discussed in Section 4.3 is investigated. A shell with L/h=10 is considered in Section 4.3. Here, two

additional cases with L/h=5 and 15 are configured to examine CODs in a comparison with the FEM solution.

The COD results for L/h=5 and 15, including u_z, θ_x, and θ_y, are illustrated in Figs. A.1 and A.2, respectively. As the same as the conclusions in Section 4.3, the COD results evaluated from Approach 3 are closest to the FEM solution than the other two approaches. It indicates that the arbitrary horizon domain method can effectively reduce the PD surface effect for shell structures with different thicknesses.

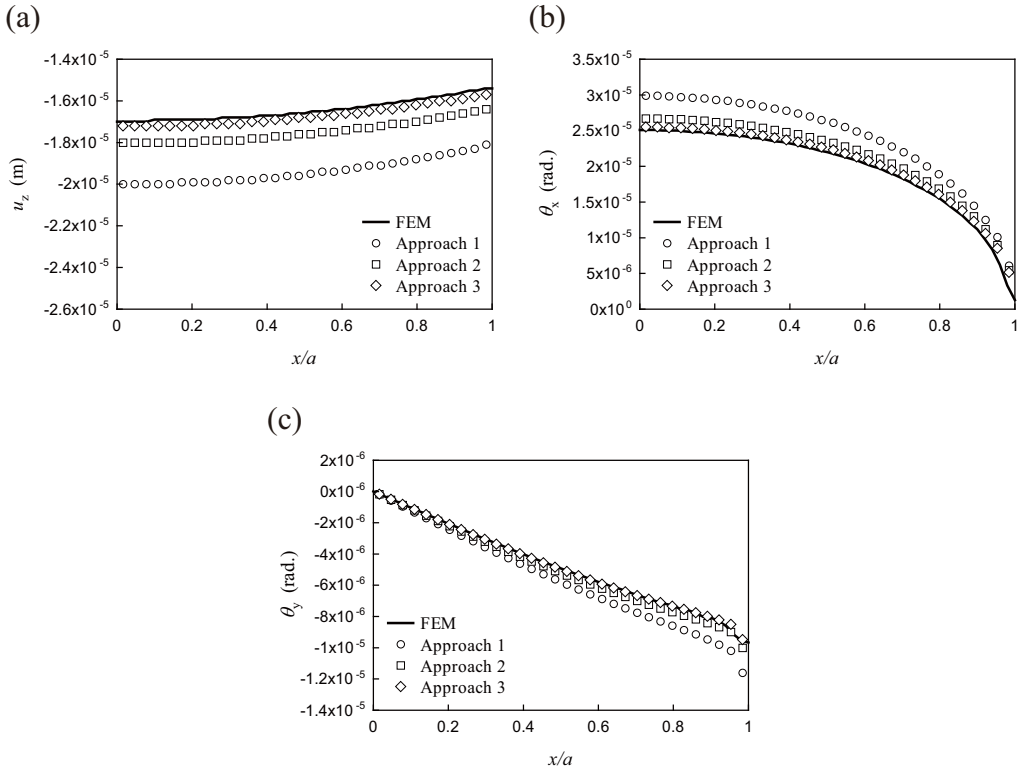

Figure A.1: Fracture mechanics quantities for L/h=5, (a) Displacement u_z, (b) Rotation θ_x, (c) Rotation θ_y.

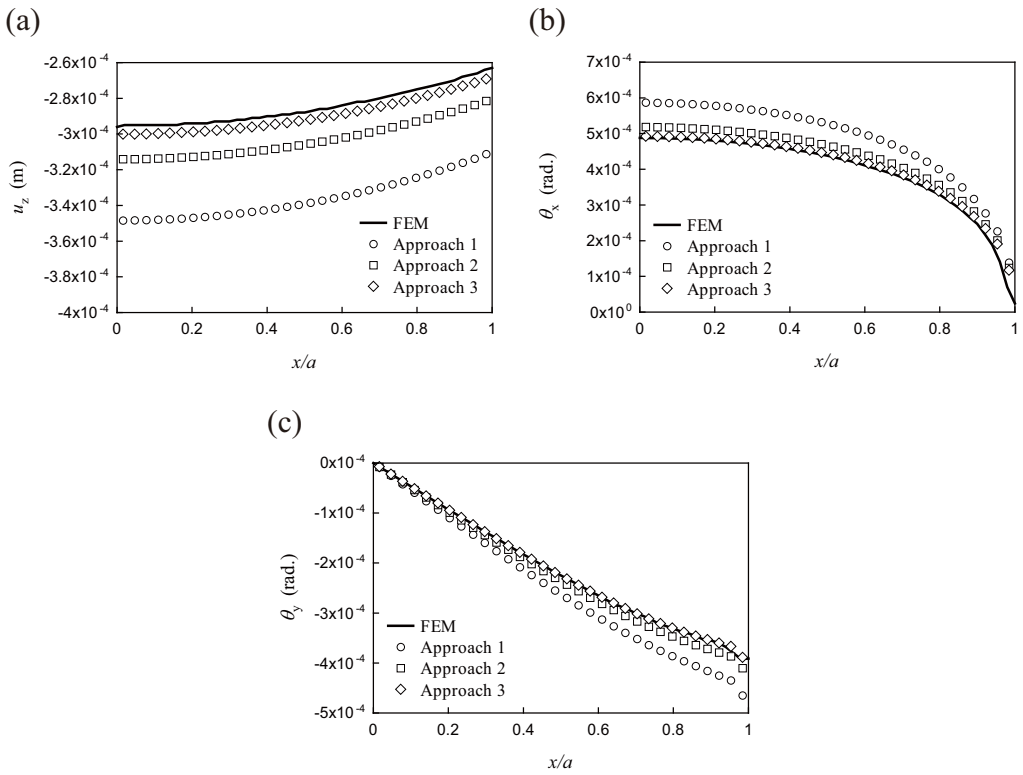

Figure A.2: Fracture mechanics quantities for L/h=15, (a) Displacement u_z, (b) Rotation θ_x, (c) Rotation θ_y.

Acknowledgements

This work was financially supported by Japan-Taiwan Exchange Association. The authors gratefully acknowledge suggestions for this study from Mr. Kuan-Chia Chen.

References
References

[1] S.A. Silling, Reformulation of elasticity theory for discontinuities and long-range forces, J. Mech. Phys. Solids 48 (2000) 175-209.

[2] S.A. Silling, M. Epton, O. Weckner, J. Xu, E. Askari, Peridynamic states and constitutive modeling, J. Elast. 88 (2007) 151-184.

[3] J. O'Grady, J. Foster, Peridynamic plates and flat shells: A non-ordinary, state-based model, Int. J. Solids Struct. 51 (2014) 4572-4579.

[4] Z. Yang, B. Vazic, C. Diyaroglu, E. Oterkus, S. Oterkus, A Kirchhoff plate formulation in a state-based peridynamic framework, Math. Mech. Solids 25 (2020) 727-738.

[5] C. Diyaroglu, E. Oterkus, S. Oterkus, E. Madenci, Peridynamics for bending of beams and plates with transverse shear deformation, Int. J. Solids Struct. 69 (2015) 152-168.

[6] C.T. Nguyen, S. Oterkus, Peridynamics for the thermomechanical behavior of shell structures, Eng. Fract. Mech. 219 (2019) 106623.

[7] S.R. Chowdhury, P. Roy, D. Roy, J.N. Reddy, A peridynamic theory for linear elastic shells, Int. J. Solids Struct. 84 (2016) 110-132.

[8] C.T. Nguyen, S. Oterkus, Ordinary state-based peridynamics for geometrically nonlinear analysis of plates, Theor. Appl. Fract. Mech. 112 (2021) 102877.

[9] J. Heo, Z. Yang, W. Xia, S. Oterkus, E. Oterkus, Buckling analysis of cracked plates using peridynamics, Ocean Eng. 214 (2020) 107817.

[10] J. Heo, Z. Yang, W. Xia, S. Oterkus, E. Oterkus, Free vibration analysis of cracked plates using peridynamics, Ships Offshore Struct. 15 (2020) 220-229.

[11] M.J. Dai, S. Tanaka, S. Oterkus, E. Oterkus, Mixed-mode stress intensity factors evaluation of flat shells under in-plane loading employing ordinary state-based peridynamics, Theor. Appl. Fract. Mech. 112 (2020) 102841.

[12] M.J. Dai, S. Tanaka, T.Q. Bui, S. Oterkus, E. Oterkus, Fracture parameter analysis of flat shells under out-of-plane loading using ordinary state-based peridynamics, Eng. Fract. Mech. 244 (2021) 107560.

[13] M. Dorduncu, Peridynamic modeling of delaminations in laminated composite beams using refined zigzag theory, Theor. Appl. Fract. Mech. 112 (2021) 102832.

[14] M. Dorduncu, K. Kaya, O.F. Ergin, Peridynamic Analysis of Laminated Composite Plates Based on First-Order Shear Deformation Theory, Int. J. Appl. Mech. 12 (2020) 2050031.

[15] C.T. Nguyen, S. Oterkus, Investigating the effect of brittle crack propagation on the strength of ship structures by using peridynamics, Ocean Eng. 209 (2020) 107472.

[16] S.A. Silling, E. Askari, A meshfree method based on the peridynamic model of solid mechanics, Comput. Struct. 83 (2005) 1526-1535.

[17] E. Madenci, S. Oterkus, Ordinary state-based peridynamics for plastic deformation according to von mises yield criteria with isotropic hardening, J. Mech. Phys. Solids 86 (2016) 192-219.

[18] J.T. Foster, S.A. Silling, W. Chen, An energy based failure criterion for use with peridynamic states, J. Multiscale Comput. Eng. 9 (2011) 675-687.

[19] D. Dipasquale, G. Sarego, M. Zaccariotto, U. Galvanetto, A discussion on failure criteria for ordinary state-based peridynamics, Eng. Fract. Mech. 186 (2017) 378-398.

[20] J. Zhao, H. Tang, S. Xue, A new fracture criterion for peridynamic and dual-horizon peridynamics, Front. Struct. Civ. Eng. 12 (2018) 629-641.

[21] H. Yu, S. Li, On energy release rates in peridynamics, J. Mech. Phys. Solids 142 (2020) 104024.

[22] T.L. Warren, S.A. Silling, A. Askari, O. Weckner, M.A. Epton, J. Xu, A non-ordinary state-based peridynamic method to model solid material deformation and fracture, Int. J. Solids Struct. 46 (2009) 1186-1195.

[23] M. Tupek, J. Rimoli, R. Radovitzky, An approach for incorporating classical continuum damage models in state-based peridynamics, Comput. Methods Appl. Mech. Eng. 263 (2013) 20-26.

[24] Q.V. Le, F. Bobaru, Surface corrections for peridynamic models in elasticity and fracture, Comput. Mech. 61 (2018) 499-518.

[25] S. Oterkus, E. Madenci, A. Agwai, Peridynamic thermal diffusion, J. Comput. Phys. 265 (2014) 71-96.

[26] A.F. Queiruga, G. Moridis, Numerical experiments on the convergence properties of state-based peridynamic laws and influence functions in two-dimensional problems, Comput. Methods Appl. Mech. Eng. 322 (2017) 97-122.

[27] K.C. Chen, The development of coupled peridynamics and isogeometric analysis method for modeling of crack propagation on ship-hull panels (Master thesis), National Taiwan Ocean University, Taiwan, 2020. (in Chinese)

[28] E. Madenci, M. Dorduncu, A. Barut, N. Phan, A state-based peridynamic analysis in afinite element framework, Eng. Fract. Mech. 195 (2018) 104-128.

[29] E. Madenci, M. Dorduncu, A. Barut, N. Phan, Weak form of peridynamics for nonlocal essential and natural boundary conditions, Comput. Methods Appl. Mech. Eng. 337 (2018) 598-631.

[30] M.R. Ayatollahi, M.R.M. Aliha, Analysis of a new specimen for mixed mode fracture tests on brittle materials, Eng. Fract. Mech. 76 (2009) 1563-1573.

[31] E. Madenci, E. Oterkus, Peridynamic theory and its applications, Springer, New York, 2014.

[32] T. Belytschko, Y.Y. Lu, L. Gu, Element-free Galerkin methods, Int. J. Numer. Methods Eng. 37 (1994) 229-256.

[33] T.L. Anderson, Fracture mechanics: fundamentals and applications, CRC Press, Boca Raton, 2004.

[34] H. Hibbitt, B. Karlsson, P. Sorensen, Abaqus analysis user's manual version 6.10, Dassault Systemes Simulia Corp, Providence, 2011.

[35] S. Liu, G. Fang, J. Liang, M. Fu, B. Wang, A new type of peridynamics: Element-based peridynamics, Comput. Methods Appl. Mech. Eng. 366 (2020) 113098.

[36] J. Chen, X. Zhou, L. Zhou, F. Berto, Simple and effective approach to modeling crack propagation in the framework of extended finite element method, Theor. Appl. Fract. Mech. 106 (2020) 102452.